

MedVL-SAM2: A unified 3D medical vision–language model for multimodal reasoning and prompt-driven segmentation

Yang Xing¹ Jiong Wu¹ Savas Ozdemir² Ying Zhang³ Yang Yang⁵
 Wei Shao⁴ Kuang Gong¹

¹Department of Biomedical Engineering, University of Florida, Gainesville, FL, USA

²Department of Radiology, University of Florida, Jacksonville, FL, USA

³Research Computing, University of Florida, Gainesville, FL, USA

⁴Department of Medicine, University of Florida, Gainesville, FL, USA

⁵Department of Radiology, UC San Francisco, San Francisco, CA, USA

Abstract

Recent progress in medical vision–language models (VLMs) has achieved strong performance on image-level text-centric tasks such as report generation and visual question answering (VQA). However, achieving fine-grained visual grounding and volumetric spatial reasoning in 3D medical VLMs remains challenging, particularly when aiming to unify these capabilities within a single, generalizable framework. To address this challenge, we proposed MedVL-SAM2, a unified 3D medical multimodal model that concurrently supports report generation, VQA, and multi-paradigm segmentation, including semantic, referring, and interactive segmentation. MedVL-SAM2 integrates image-level reasoning and pixel-level perception through a cohesive architecture tailored for 3D medical imaging, and incorporates a SAM2-based volumetric segmentation module to enable precise multi-granular spatial reasoning. The model is trained in a multi-stage pipeline: it is first pre-trained on a large-scale corpus of 3D CT image–text pairs to align volumetric visual features with radiology-language embeddings. It is then jointly optimized with both language-understanding and segmentation objectives using a comprehensive 3D CT segmentation dataset. This joint training enables flexible interaction via language, point, or box prompts, thereby unifying high-level visual reasoning with spatially precise localization. Our unified architecture delivers state-of-the-art performance across report generation, VQA, and multiple 3D segmentation tasks. Extensive analyses further show that the model provides reliable 3D visual grounding, controllable interactive segmentation, and robust cross-modal reasoning, demonstrating that high-level semantic reasoning and precise 3D localization can be

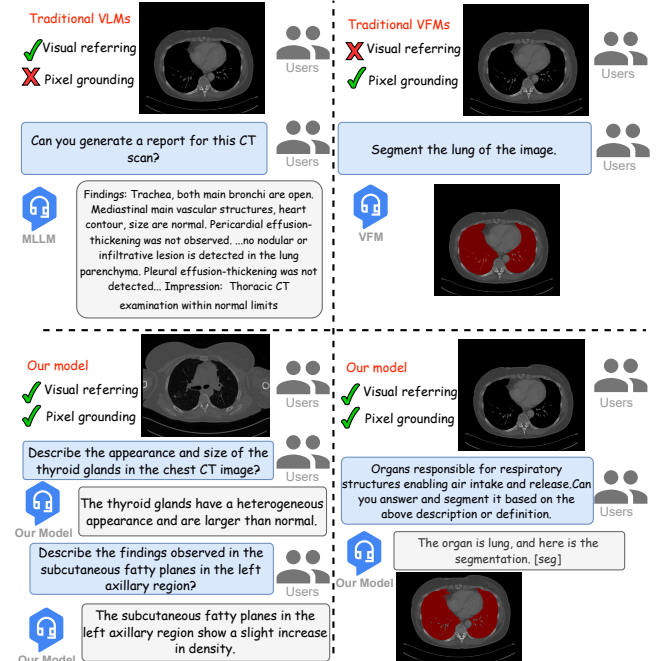


Figure 1. Comparison of the proposed model to traditional text-response-only medical vision-language models (VLMs) and mask-response-only medical vision foundation models (VFM).

jointly achieved within a unified 3D medical VLM.

1. Introduction

Leveraging large-scale radiology image-text pairs, medical vision–language models (VLMs) exhibit strong reasoning ability over both global image semantics and clinical narratives. Furthermore, several studies have incorporated vi-

sual grounding into VLMs, enabling them to spatially localize disease-related regions or anatomical structures referenced in language prompts. However, the reliance on 2D vision-language architectures inherently constrains their effectiveness in 3D medical image analysis. Specifically, 2D VLMs lack volumetric perception and spatial consistency across slices, both of which are essential for understanding complex 3D structures such as tumors, vessels, and organs. Consequently, while 2D grounding may localize features within an individual slice, it fails to capture the spatial continuity, anatomical context, and morphological variations present across the full 3D volume.

Recent efforts have begun to explore 3D medical VLMs, such as Med3DVLM [46] and CT-Chat [9], which process volumetric data and generate textual outputs. Nevertheless, these models remain limited to language-only output, lacking pixel-level grounding or segmentation capabilities, which restricts their applicability in clinically meaningful interpretation and interaction. A significant gap thus remains in developing 3D medical VLMs capable of comprehensive visual grounding and aligning textual concepts with 3D spatial regions. To address this, several grounded 3D VLMs have been proposed, including M3D [2] and VILA-M3 [30]. M3D incorporated 3D information but is constrained by the low input resolution of its vision encoder and the design of its projection layer, both of which introduce substantial volumetric information loss. Meanwhile, VILA-M3 relies on domain-specific expert modules for downstream tasks, and its performance may become unstable when these components are not effectively activated. These limitations underscore the need for a unified 3D medical VLM capable of understanding volumetric image structures while preserving strong language–vision alignment.

To address these challenges, we propose MedVL-SAM2, a unified 3D medical VLM that extends a LLaVA-style architecture to incorporate volumetric perception and multi-modal reasoning. Fig. 1 illustrates the differences of our model compared to traditional medical vision-language models (VLMs) and vision foundation models (VFs). MedVL-SAM2 incorporates image-level understanding and pixel-level segmentation within a single framework, enabling both high-level language-driven analysis and fine-grained spatial localization. Specifically, our model integrates the prompt-driven paradigm of SAM2 into a 3D vision-language backbone, supporting multi-modal interaction through language, point, and bounding-box prompts. Our key contributions are summarized as follows:

- The proposed model provides a unified 3D medical VLM capable of jointly performing image-level reasoning and pixel-level perception, supporting report generation, VQA, and multiple types of 3D segmentation.
- The framework incorporates multi-modal prompting through language, point, and bounding-box inputs, enabling flexible and interactive 3D image segmentation.

Table 1. Capability comparison between our model and current state-of-the-art methods across report generation (RG), visual question answering (VQA), semantic segmentation (SS), referring segmentation (RS), and interactive segmentation (IS).

Method	RG	VQA	SS	RS	IS
BiomedParse [55]	✗	✗	✓	✓	✗
medSAM2 [28]	✗	✗	✓	✗	✓
CT-CHAT [9]	✓	✓	✗	✗	✗
Med3DVLM [46]	✓	✓	✗	✗	✗
Med-2E3 [38]	✓	✓	✗	✗	✗
MS-VLM [15]	✓	✓	✗	✗	✗
M3D [2]	✓	✓	✓	✓	✗
Ours	✓	✓	✓	✓	✓

- The method achieves superior performance on two large-scale benchmarks, consistently surpassing current approaches in both reasoning and segmentation tasks.

2. Related Works

2.1. Vision-Language Models (VLMs)

Vision-language models (VLMs) integrate visual encoders with LLMs for vision-language understanding. Early approaches rely on complex fusion mechanisms, such as cross-attention (Flamingo [1]) and query transformers (BLIP-2 [20]), while more recent approaches have converged toward simpler, unified designs. LLaVA [17, 24] shows that a vision encoder with a linear projection is sufficient for effective vision-language alignment, leading to numerous extensions (LLaVA-Next [19], VILA [22], InternVL [6]), and recent unified foundation models (GPT-5 [31], Gemini2.5 [7], Qwen3 [48]). While these models excel in text generation and high-level reasoning, they lack inherent spatial grounding capabilities. Recent works have integrated pixel-level localization through segmentation adapters (LISA [13], VISA [47]), region encoders (GLaMM [34], Ferret [50, 53]), and multi-prompt frameworks (SA2VA [51]). However, these grounding-enabled VLMs operate solely on 2D images or videos and cannot process 3D volumetric medical data.

2.2. Medical VLMs

The integration of multimodal reasoning into medical imaging has led to rapid progress in medical VLMs for report generation and VQA. Early efforts such as LLaVA-Med [18] and Med-Flamingo [29] adapt general-purpose multimodal frameworks to radiology datasets, enabling report generation and VQA. Subsequently, HuatuoGPT-Vision [52], HealthGPT [23], MedTrinity [45], and RadFM [43] extend this line of work by coupling visual-language reasoning with radiology-specific representations to improve clinical understanding. More recent models,

including MIMO [5] and MedPLIB [11], improve fine-grained visual grounding through language-guided segmentation and pixel-level reasoning. However, all these models are constrained to 2D slice-based analysis and cannot capture volumetric spatial continuity, which is essential for accurate 3D medical reasoning. To address this limitation, several models have advanced toward volumetric understanding. CT-Chat [9] and Med3DVLM [46] align 3D CT embeddings with radiology reports for volumetric text generation but lack segmentation or grounding. VividMed [25], MS-VLM [15] and Med-2E3 [38] extended CT-CHAT model by integrating both 3D and 2D features, but still restricted to text-only tasks. M3D [2] introduces segmentation heads for spatial reasoning but suffers from information loss caused by the compression of input image dimension and projection layer, while ViLA-M3 [30] employs an agent-triggered segmentation mechanism that highly depended on explicit token activation.

2.3. Vision Foundation Models

The Segment Anything Model (SAM) [12] and SAM2 [35] establish universal segmentation capabilities through multi-prompt interaction (points and boxes). Their strong zero-shot generalization abilities has motivated adaptations to the medical domain [4, 37]: MedSAM [27] and MedSAM2 [28] fine-tune SAM architectures on radiology datasets, while SAM-Med3D [49], SegVol [8], and parameter-efficient adapters [44] extend these models to 3D volumetric data. Additional efforts such as UniSeg [3] and BiomedParse [55] further broaden biomedical segmentation across multiple imaging modalities. Despite their strong perceptual capability, these VFM remain segmentation-oriented and lack language-guided reasoning. Our framework addresses this gap by integrating SAM2’s promptable segmentation within a LLaVA-style 3D medical VLM backbone, combining precise mask generation with semantic understanding to enable unified 3D volumetric reasoning and interactive segmentation. A comparison of task coverage across existing SOTA 3D medical VLMs, VFM, and our model is provided in Table 1.

3. Methods

3.1. Problem definition

3D medical vision–language tasks cover a broad spectrum, including report generation, VQA, referring segmentation, and interactive segmentation. To support all these tasks within a single model, we introduce a unified formulation that accommodates both text-centric and mask-centric predictions. Given a 3D medical volume $\mathcal{I}_{in} \in \mathbb{R}^{X \times Y \times Z}$ with size of $X \times Y \times Z$, a sequence of text tokens $\mathcal{T}_{in} \in \mathbb{R}^{N \times D}$ with size of $N \times D$, and a set of prompt tokens \mathcal{P}_{in} , the

unified multi-task problem can be formulated as

$$(\mathcal{T}_{out}, \mathcal{M}_{out}) = \mathcal{F}(\Theta; \mathcal{I}_{in}, \mathcal{T}_{in}, \mathcal{P}_{in}), \quad (1)$$

where $\mathcal{F}(\cdot)$ denotes the unified 3D medical VLM, $\Theta = \{\theta_{vbl}, \theta_{seg}\}$ denotes the trainable parameters including the vision-language backbone parameters θ_{vbl} and the segmentation module parameters θ_{seg} , \mathcal{T}_{out} represents the output text tokens, and \mathcal{M}_{out} is the output segmentation mask. The output text tokens \mathcal{T}_{out} are decoded by the tokenizer to generate the text output. Different from the current unified medical VLMs, our method provides visual prompts \mathcal{P}_{in} to enhance interactive segmentation. Here \mathcal{P}_{in} includes the bounding box prompt \mathcal{P}_{bbox} and the point prompt \mathcal{P}_{pt} .

3.2. Architecture Overview

As shown in Fig. 2, our approach consists of a LLaVA-like VLM and a promptable segmentation module. The VLM comprises the following components: (i) a volumetric vision encoder, (ii) an adaptive token projection layer, and (iii) an LLM backbone with LoRA layers. Our architecture addresses three key challenges in unified 3D medical VLM design: **Challenge 1: Volumetric Understanding.** Unlike 2D VLMs, 3D medical imaging requires capturing spatial relationships across slices. We address this through a 3D-aware vision encoder (M3D-CLIP) that preserves volumetric context. **Challenge 2: Computational Efficiency.** Direct encoding of 3D volumes produces 2048 visual tokens per image (fourfold more than 2D LLaVA), causing prohibitive LLM inference costs. We address this via a MLP_Mixer projection layer that reduces tokens to 512 while preserving spatial information. **Challenge 3: Cross-Slice Consistency.** Unlike 2D segmentation where each image is independent, 3D segmentation requires anatomical continuity across slices. To alleviate this issue, the proposed model leverages the memory attention mechanism of SAM2 to maintain slice-wise consistency throughout the volume.

3.3. Vision-Language Processing Pipeline

Volumetric vision encoder. Following the design of LLaVA, a CLIP-based 3D encoder [33] is adopted as the vision encoder. Given an input 3D volume \mathcal{I}_{in} , the image embeddings v_{in} are derived via a 3D CLIP-based encoder E_{vc} resulting in $v_{in} = E_{vc}(\mathcal{I}_{in}) \in \mathbb{R}^{n \times d}$, where n is the number of visual tokens and d is the token dimension. In our framework, model weights from the pre-trained 3D vision-transformer (3D ViT) [2] are utilized.

Adaptive token projection layer. The high spatial dimensionality of 3D medical images leads to very large token sequences after ViT patch embedding. In 3D CLIP, a $32 \times 256 \times 256$ volume is partitioned into $8 \times 16 \times 16$ patches, producing 2,048 visual tokens, which results in a four-fold increase in inference time compared with the

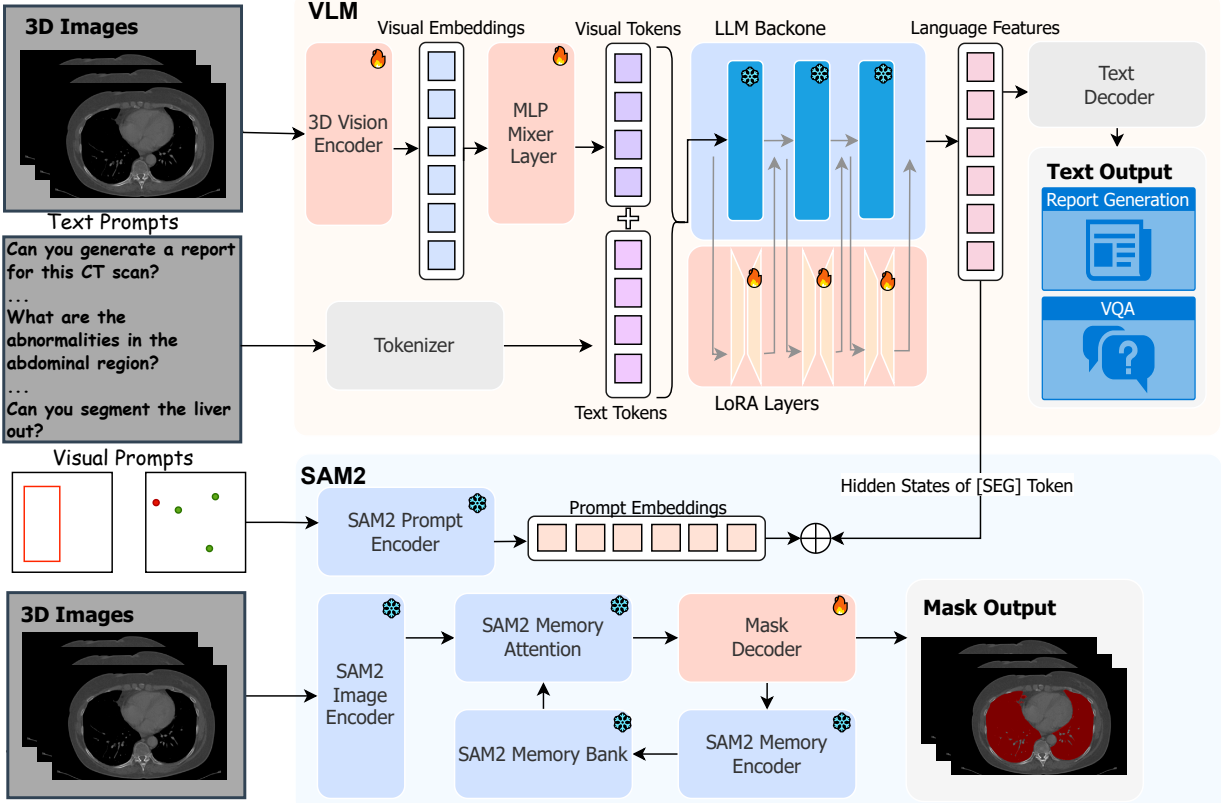


Figure 2. Overview of the proposed architecture, which integrates a LLaVA-style VLM with a SAM2-based segmentation module. The VLM processes 3D volumes and generates text autoregressively. When a [SEG] token is produced, its hidden state is extracted and fed into SAM2’s prompt encoder, where it is fused with optional visual prompts (points or boxes) to generate the final segmentation mask.

512-token LLaVA model. Furthermore, because anatomical structures occupy only a small portion of the volume, most visual tokens correspond to background regions, making direct processing of all tokens highly inefficient.

To address this issue, we introduce two MLP-Mixer layers [39] as a projector that compresses the visual tokens from 2,048 to 512 with minimal information loss. Each MLP-Mixer layer contains two fully connected sublayers with nonlinearities applied independently to each row of the input tensor: the first performs channel mixing, and the second performs token mixing. Omitting layer indices, the mixer layer is formulated as

$$U^T = W_2 \sigma(W_1 \text{LayerNorm}(v_{in}^T)), \quad (2)$$

$$T_v = W_4 \sigma(W_3 \text{LayerNorm}(U)),$$

where σ denotes the GELU activation function, $U \in \mathbb{R}^{\hat{n} \times \hat{d}}$ and $T_v \in \mathbb{R}^{\hat{n} \times \hat{d}}$ are the visual tokens aligned with the LLM’s text embedding dimensions ($\hat{n} = 512$ and $\hat{d} = 2048$ in our case). The computational complexity of the MLP-Mixer layer is linear with respect to the number of input patches, which enables efficient compression of 3D volumetric embeddings while preserving spatial information.

LLM backbone with LoRA. In our model, InternVL-2.5-4B [6] is utilized as the LLM backbone for its strong multimodal understanding and text generation capabilities. LoRA [10] layers are applied to the query, key, and value projection matrices in all transformer layers to enable efficient fine-tuning. The overall process is formulated as: $T_{out} = LLM(T_{in} + T_v)$, where T_{in} denotes the tokenized text prompt and T_v denotes the visual tokens produced by the projection layer.

3.4. [SEG] Token Controlled Segmentation

In our framework, SAM2 is employed as the segmentation module for its strong performance and native support for multi-prompt interaction. The 3D medical volume is processed slice-by-slice using memory attention to maintain cross-slice consistency. Pixel-level grounding is enabled through a hidden state of [SEG] token, denoted as $[SEG]_{hs}$, which serves as a semantic prompt and complements geometric prompts such as points and bounding boxes. Specifically, $[SEG]_{hs}$ is passed to the SAM2 decoder, where it is concatenated with prompt embeddings from the SAM2 prompt encoder and decoded into segmen-

tation masks. During training, the SAM2 decoder learns to interpret the spatial-temporal prompt, while gradients flowing through the [SEG] token enable the VLM to learn how to use it for accurate grounding. The segmentation module can be denoted as $\mathcal{M}_{out} = SAM2(\mathcal{I}_{in}, [\text{SEG}]_{hs}, \mathcal{P}_{in})$. A unidirectional design is adopted in which SAM2 outputs are not fed back into the LLM, allowing the architecture to remain simple, minimizing cross-modal alignment overhead, and enabling independent module upgrades.

4. Implementation Details

4.1. Datasets

CT-RATE. To evaluate report generation and VQA performance, we utilize the CT-RATE dataset [9], a large-scale, public resource comprising 21,304 3D non-contrast chest CT volumes paired with corresponding free-text radiology reports and over 2.7 million VQA pairs. The dataset is officially partitioned into a training set of 20,000 patients and a test set of 1,304 patients. For report generation, the “Findings” and “Impression” sections are extracted from the original radiology reports and used as ground truth. A comprehensive instruction-tuning dataset derived from the CT-RATE reports is employed for VQA, which is specifically structured to cover three distinct question-answer formats, including short answers, long answers, and multiple-choice questions, to evaluate the robustness of the model’s interactive and diagnostic reasoning capabilities.

M3D-Seg. The M3D-Seg dataset [2] is used to evaluate 3D segmentation performance. M3D-Seg is a unified benchmark that aggregates 3D CT scans from 25 public segmentation datasets, providing 5,772 labeled volumes paired with 119,267 category text descriptions and segmentation masks covering 211 anatomical structures. For interactive segmentation, we generate point and bounding-box prompts following the MedSAM2 protocol: three positive points are randomly sampled within the target region, and boxes are derived from the ground-truth masks with $\pm 5\%$ spatial jitter to simulate imperfect user input.

4.2. Multi-Stage Training

Inspired by Cambrian-1 [40] framework, we employ a three-stage progressive training strategy to stably align 3D visual features, language representations, and spatial grounding. In the first stage, only the MLP-Mixer projection layer is optimized, while the vision encoder, LLM, and SAM2 modules remain frozen. This stage establishes the initial vision-language alignment and is trained for 3 epochs on the report-generation subset of CT-RATE using the autoregressive language modeling loss \mathcal{L}_{text} [51]. In the second stage, the trainable set is expanded to include the vision encoder, the projection layer, and the LLM LoRA parameters, with SAM2 still frozen. This stage focuses on strength-

Table 2. Performance comparison on report generation.

Method	BLEU-1	ROUGE	METEOR	CIDEr	BERTScore
LLaVA [24]	18.47	10.34	11.22	0.050	30.55
CXR-LLaVA [16]	9.12	5.05	2.86	0.049	39.18
LLaVA-Med [18]	9.01	5.24	2.24	0.006	40.65
M3D [2]	14.49	19.25	14.11	0.081	84.12
CT-CHAT [9]	43.64	31.57	23.06	0.221	88.12
Ours	41.85	34.59	22.15	0.237	89.33

ening language reasoning and is trained for 5 epochs on CT-RATE, sampling report-generation, and VQA tasks with equal probability under the same objective \mathcal{L}_{text} . In the final stage, the SAM2 decoder is unfrozen to enable full multimodal grounding. Joint optimization is performed for 5 epochs using both the CT-RATE and the M3D-Seg datasets using the composite objective function

$$\mathcal{L}_{joint} = \lambda_{text} \mathcal{L}_{text} + \lambda_{mask} (\mathcal{L}_{CE} + \lambda_{Dice} \mathcal{L}_{Dice}), \quad (3)$$

where \mathcal{L}_{CE} is the voxel-wise binary cross-entropy loss, \mathcal{L}_{Dice} denotes the Dice loss. Coefficients λ_{text} , λ_{mask} , and λ_{Dice} control the relative contributions of each term. This staged training schedule reduces catastrophic forgetting, stabilizes optimization, and results in a unified model capable of robust text-mask grounding. Further training details may be found in Sec. 8.

5. Experiments

5.1. Evaluation on Report Generation

We evaluate report generation on the CT-RATE test set, which contains 1,304 CT-report pairs. Traditional n-gram-based NLP metrics and LLM-based metrics are used for assessment, including BLEU [32], ROUGE [21], METEOR [14], CIDEr [41], and BERTScore [54]. While n-gram metrics capture lexical overlap, they offer limited semantic insight. In contrast, LLM-based metrics assess a deeper semantic similarity between the generated reports and the ground-truth findings. We compare our model with representative multimodal baselines, including LLaVA [24], CXR-LLaVA [16], LLaVA-Med [18], M3D [2], and CT-Chat[9]. All models are evaluated under identical inference conditions. The results are presented in Tab. 2. Our model achieves strong performance across both traditional and LLM-based evaluation metrics. Specifically, it outperforms 2D medical multimodels such as LLaVA, CXR-LLaVA, and LLaVA-Med by large margins, indicating better textual fluency and clinical content accuracy. Compared with 3D baselines, our model significantly surpasses M3D and achieves comparable or higher scores than the current state-of-the-art CT-Chat, demonstrating improved semantic fidelity and reasoning ability in the volumetric report generation task.

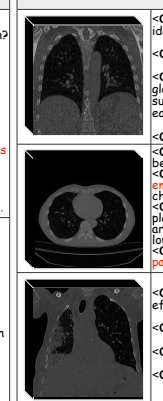
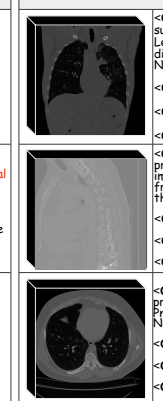
Long Answer	Short Answer	Multiple Choice
<p>Long Answer</p> <p><Question>: Describe the findings observed in the subcutaneous fatty planes in the left axillary region?</p> <p><Ground Truth>: Heterogeneous density increases were observed in the subcutaneous fatty planes in the left axillary region (secondary to post-treatment?).</p> <p><CT-CHAT>: A few millimetric nonspecific lymph nodes are observed in the subcutaneous fatty planes in the left axillary region.</p> <p><Our model>: The subcutaneous fatty planes in the left axillary region show a slight increase in density.</p> <p><Question>: Describe the appearance of the gallbladder at the fundus level.</p> <p><Ground Truth>: Density compatible with a 3.5 mm diameter calculus is observed at the fundus level in The gallbladder.</p> <p><CT-CHAT>: The gallbladder has a hypodense appearance with increased wall thickness and a hyperdense appearance that may be compatible with mud-calculus.</p> <p><Our model>: The gallbladder at the fundus level has a dense appearance, which may be compatible with gallstones</p> 	<p>Short Answer</p> <p><Question>: What kinds of anomalies can be identified in the scan?</p> <p><Ground Truth>: viral pneumonia</p> <p><CT-CHAT>: The scan shows patchy ground glass opacity in the right lung lower lobe superior segment, which may be indicative of early infectious process or atelectasis.</p> <p><Our model>: viral pneumonia</p> <p><Question>: What kinds of abnormalities can be identified in the scan?</p> <p><Ground Truth>: pulmonary nodules, paraseptal emphysema, centrilobular emphysema</p> <p><CT-CHAT>: There are calcified atherosoma plaques in the thoracic aorta and coronary arteries, and a sliding type hiatal hernia at the esophageal hiatus.</p> <p><Our model>: centrilobular emphysema, paraseptal emphysema, pulmonary nodules</p> <p><Question>: What is the measurement of the effusion detected in the thoracic cavity?</p> <p><Ground Truth>: 33 mm</p> <p><CT-CHAT>: 27 mm</p> <p><Our model>: 32 mm</p> 	<p>Multiple Choice</p> <p><Question>: What is the size of the nonspecific lymph nodes observed in both lungs? (a) Less than 5 mm in diameter (b) 5-10 mm in diameter (c) More than 10 mm in diameter (d) Not specified</p> <p><Ground Truth>: (a) Less than 5 mm in diameter</p> <p><CT-CHAT>: (d) Not specified</p> <p><Our model>: (a) Less than 5 mm in diameter</p> <p><Question>: Which of the following findings are present in the bone structures of this Chest CT image? (a) Lytic bone lesions (b) Pathological fracture (c) Cement material placement (d) All of the above</p> <p><Ground Truth>: (d) All of the above</p> <p><CT-CHAT>: (c) Cement material placement</p> <p><Our model>: (d) All of the above</p> <p><Question>: Which of the following findings are present in the lung parenchyma window? (a) Pneumonia (b) Emphysematous changes (c) Normal lung parenchyma (d) Both a and c</p> <p><Ground Truth>: (b) Emphysematous changes</p> <p><CT-CHAT>: (d) Both a and c</p> <p><Our model>: (b) Emphysematous changes</p> 

Figure 3. Comparison between the proposed methods to CT-CHAT on VQA tasks, including Long Answer, Short Answer, and Multiple choice subsets. Critical clinical information were highlighted in red. For CT-CHAT, the input question additionally contained a special token ([short_answer], [long_answer], [multiple_choice]) to indicate the specific subset to evaluate.

5.2. Evaluation on VQA

We evaluated VQA performance on the CT-RATE dataset, which includes three subtasks: long-answer, short-answer, and multiple-choice VQA. Qualitative examples are shown in Fig. 3. The long-answer and short-answer subtasks are treated as open-ended VQA, where the model generates free-form responses, while the multiple-choice subtask is treated as closed-ended VQA, where the model selects one answer from predefined options. For open-ended tasks, we employ BLEU, ROUGE, METEOR, CIDEr, and LLM score to evaluate lexical and semantic similarity between generated and reference answers. For the closed-ended task, accuracy is used as the measure. Based on the findings from the report-generation experiments, which reveal that 2D medical multimodels such as LLaVA, CXR-LLaVA, LLaVA-Med, and 3D multimodel M3D exhibit substantial performance limitations, we focus our comparison on the current state-of-the-art CT-Chat model. Quantitative results are presented in Table 3. Our model achieves comparable or superior performance across all VQA subtasks. It delivers consistent improvements in ROUGE, LLMscore, and accuracy, indicating stronger semantic alignment and reasoning capabilities. Notably, our model achieves 89.74% accuracy on multiple-choice VQA, surpassing CT-Chat by a clear margin. These results confirm that incorporating prompt-driven segmentation and volumetric understanding enhances multimodal reasoning and overall comprehension in both open-ended and closed-ended 3D medical VQA tasks.

5.3. Evaluation on Referring Segmentation

We evaluated referring segmentation on the M3D_Seg test set using the same data split as the M3D model. Since no other existing models support referring segmentation for 3D

medical volumes, we use only SegVol and M3D as baseline methods. Performance is reported on three benchmark subsets of M3D_seg dataset, including CTOrg [36], Abdomen-CT-1K (ACT-1K) [26], and Total Segmentor (TS) [42], using the Dice coefficient as the evaluation metric. For referring segmentation, the text prompt is a randomly selected free-form description of the target region that excludes explicit class names, allowing us to evaluate the model’s ability to perform language-driven spatial reasoning. To further assess the reasoning capabilities of our model, we additionally evaluate performance on semantic segmentation, where the text prompt explicitly specifies the anatomical class (e.g., “segment the liver”). Example prompts are provided in Sec. 9 and quantitative results are shown in Tab. 4. Across all subsets, our model achieves the highest Dice scores in both referring and semantic segmentation. Compared to SegVol, which relies solely on volumetric features, our model improves Dice by at least 10 percent for each dataset. When compared to M3D, our approach achieves consistent gains of around 5 percent, demonstrating stronger spatial reasoning and text-conditioned localization abilities. Notably, our referring segmentation performance is comparable to semantic segmentation, indicating that the model can accurately localize anatomical structures from implicit textual descriptions without explicit class labels. Overall, these results validate the effectiveness of our unified 3D multimodal framework for language-guided volumetric segmentation. The integration of prompt-driven SAM2 segmentation with multimodal reasoning enables precise and interpretable 3D spatial ground truth crucial for clinical workflows involving complex 3D anatomical structures.

Table 3. Comparison between CT-CHAT and our model on long-answer, short-answer, and multiple-choice VQA tasks.

Task	Long Answer					Short Answer					Multiple Choice
	BLEU	ROUGE	METEOR	CIDEr	BERTScore	BLEU	ROUGE	METEOR	CIDEr	BERTScore	
CT-CHAT [9]	47.020	48.450	28.200	2.910	90.140	27.460	45.590	15.470	1.652	90.120	83.730
Ours	45.941	48.983	28.218	2.861	92.760	24.076	57.428	14.026	1.771	92.503	89.741

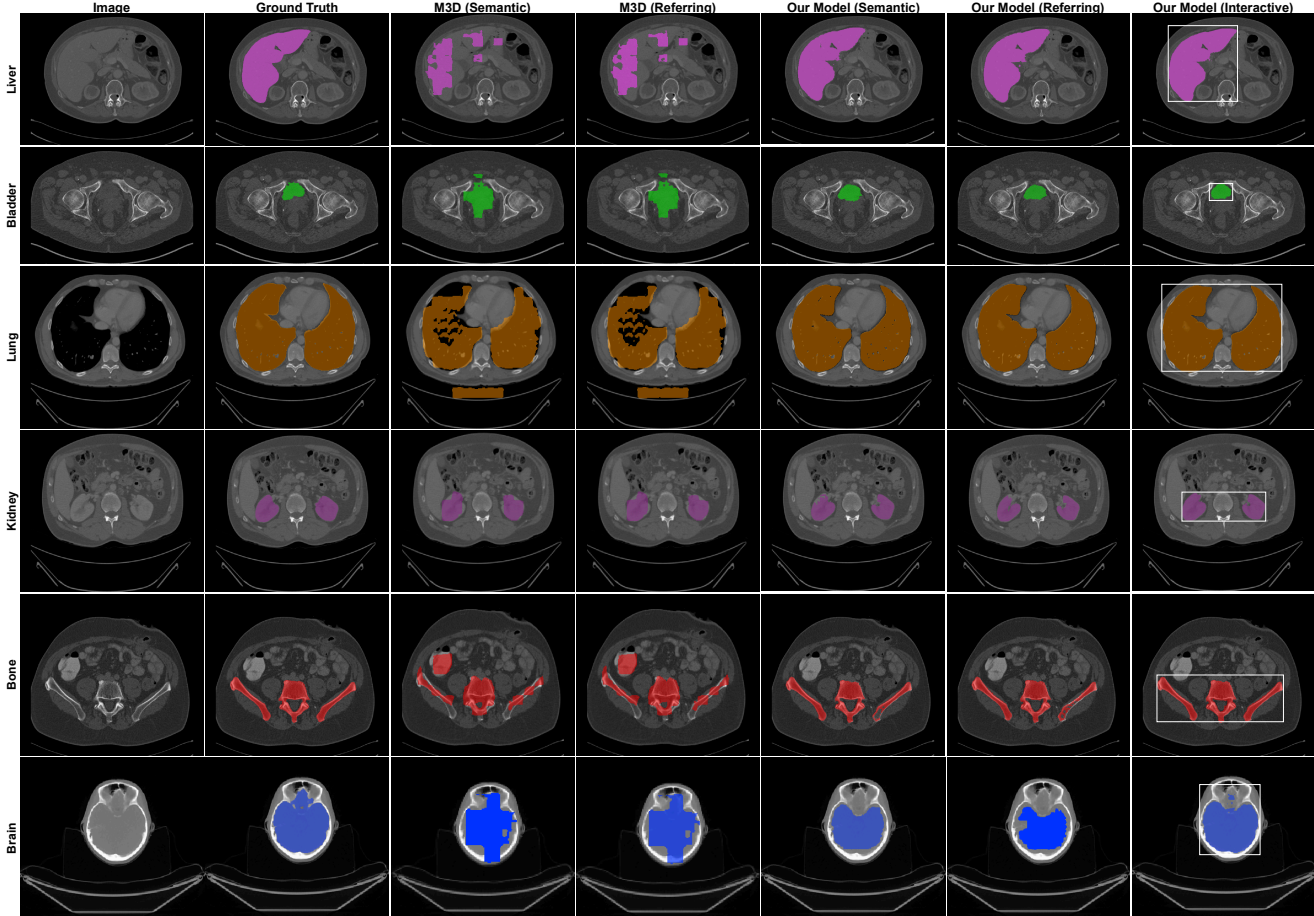


Figure 4. Comparison of the proposed method with M3D on referring and semantic segmentation. Interactive segmentation results using bounding-box prompts are also included for comparison (CTOrg dataset shown). Liver is shown in magenta, bladder in green, lung in brown, kidney in purple, bone in red, and brain in blue.

5.4. Evaluation on Interactive Segmentation

We further evaluate interactive segmentation on the same dataset and testing protocol as in the referring segmentation experiments. This setting simulates a human-in-the-loop workflow, in which users iteratively refine segmentation masks through additional prompts. Two interaction modes are examined: bounding-box prompting and point prompting. For bounding-box prompting, a random slice is selected from each 3D volume, and a bounding box with slight spatial jitter from the ground truth is provided as input. For point prompting, three randomly sampled posi-

tive points within the target region are selected on a random slice. In both settings, the model receives the same image and text inputs as in referring segmentation, augmented with the corresponding visual prompts. Dice coefficient is used as the evaluation metric. Since no existing 3D medical VLMs support interactive segmentation with text-based prompts, our semantic and referring segmentation results serve as baselines. Quantitative results are summarized in Table 5, and qualitative examples for both referring and interactive segmentation are shown in Fig. Fig. 4. Across all datasets, both interactive variants consistently

Table 4. Results on the referring segmentation task.

Method	CTOrg	ACT-1K	Total Segmentor
SegVol [8]	77.78	79.06	44.28
M3D [2] (semantic)	81.27	73.64	58.30
M3D [2] (referring)	83.49	73.63	58.50
Ours (semantic)	88.04	88.27	66.23
Ours (referring)	87.93	88.34	66.50

Table 5. Results on the interactive segmentation task.

Method	CTOrg	ACT-1K	Total Segmentor
Ours (semantic)	88.04	88.27	66.23
Ours (referring)	87.93	88.34	66.50
Ours (bbox prompt)	88.76	88.71	70.51
Ours (points prompt)	88.52	88.49	69.88

outperform their non-interactive baselines. Bounding-box prompts yield the highest Dice scores, followed by point prompts. These findings demonstrate that incorporating user feedback substantially improves segmentation quality.

We also observe that interactive refinement yielded modest improvements on CTORG and ACT-1K. Both datasets consist primarily of large, well-defined organs (e.g., liver, lungs, kidneys), for which the language-driven [SEG] token already encodes rich spatial and semantic cues from the volumetric context. As a result, adding point or bounding-box prompts provides only incremental gains, since the model can infer coarse boundaries directly from language descriptions. In contrast, results on the TotalSegmentor dataset exhibit a larger improvement. This dataset is considerably more challenging, as it contains numerous small and complex anatomical structures, such as vertebrae, ribs, and vessels. For these fine-grained regions, the global language representation may lack sufficient spatial specificity, leading to under- or over-segmentation when relying solely on text. In these cases, explicit interactive prompts supply critical spatial priors, enabling the model to localize small anatomical regions more precisely. Overall, these findings highlight the complementary role of interactive segmentation in clinical workflows: while large structures can often be segmented reliably from language alone, small or complex anatomical targets benefit significantly from user-guided refinement, making the model more practical and adaptable for real-world clinical workflows.

6. Ablation Studies

6.1. Impact of Vision Encoder and Projection Layer

To assess the contributions of the vision encoder and projection layer, we conduct ablation experiments on the CTORG and ACT-1K subsets using the interactive segmen-

Table 6. Ablation studies on different choices of vision encoders and projection layers.

Vision Encoder	Projection Layer	CTOrg	ACT-1K
Vanilla CLIP [33]	Linear	30.18	44.65
M3D-CLIP [2]	Linear	61.99	74.58
M3D-CLIP [2]	MLP	77.78	79.83
M3D-CLIP [2]	MLP_Mixer	88.04	88.27

tation task. As shown in Table 6, two vision encoders are compared: vanilla CLIP and M3D-CLIP. For the projection layer, we evaluate three configurations: Linear, MLP, and MLP-Mixer. Replacing the vanilla CLIP encoder with the M3D CLIP backbone results in a substantial improvement in Dice scores, highlighting the importance of volumetric-aware pretraining for 3D medical data. The M3D CLIP encoder effectively captures cross-slice spatial context and anatomical continuity, while the vanilla CLIP model trained on natural images lacks such volumetric priors. Projection-layer design also has a notable impact. Linear and MLP projectors offer limited cross-modal alignment, resulting in weaker performance. In contrast, the MLP-Mixer achieves the highest Dice scores, indicating that its ability to jointly model spatial and channel-wise interactions enables richer multimodal fusion and more effective volumetric reasoning. Overall, these findings validate our architectural choices: M3D-CLIP provides strong 3D semantic representations, and the MLP-Mixer projection layer facilitates robust vision–language alignment, jointly leading to significant gains in both referring and interactive segmentation tasks.

6.2. Impact of Multi-Stage Training Strategy

To evaluate the effectiveness of our multi-stage training approach, we compare it with an alternative one-stage end-to-end training strategy, where all components are trained simultaneously from scratch. Both strategies are evaluated on the CT-RATE dataset for the report generation task, using BLEU-1, ROUGE, METEOR, and CIDEr as evaluation metrics. Quantitative results are shown in Table 7. The multi-stage training strategy consistently outperforms one-stage end-to-end training across all metrics. The one-stage approach exhibits suboptimal convergence, as the simultaneous optimization of multiple large modules under competing cross-modal objectives hinders stable alignment between visual and language representations. In contrast, the progressive training schedule provides clear optimization phases, facilitating more reliable vision–language alignment. These results validate the use of a progressive multi-stage training pipeline.

Table 7. Ablation studies on different choices of training strategies.

Training strategy	BLEU-1	ROUGE	METEOR	CIDEr
One-stage	38.58	32.53	20.89	20.95
Multi-stage	41.85	34.59	22.15	23.71

7. Conclusion

In this work, we introduce MedVL-SAM2, a unified 3D VLM that integrates SAM2’s promptable segmentation with a LLaVA-style multimodal framework. The model jointly supports report generation, VQA, and semantic, referring, and interactive segmentation, bridging image-level reasoning with pixel-level perception. Extensive experiments demonstrate state-of-the-art performance across multiple 3D benchmarks, confirming MedVL-SAM2’s strengths in volumetric reasoning, 3D visual grounding, and interactive segmentation.

References

- [1] Jean-Baptiste Alayrac and et al. Flamingo: a visual language model for few-shot learning. *arXiv preprint arXiv:2204.14198*, 2022. 2
- [2] Fei Bai, Yicheng Du, and Thomas Huang. M3d: Advancing 3d medical image analysis with multi-modal large language models. *arXiv preprint arXiv:2407.07846*, 2024. 2, 3, 5, 8
- [3] Victor Ion Butoi, Jose Javier Gonzalez Ortiz, Tianyu Ma, Mert R. Sabuncu, John Guttag, and Adrian V. Dalca. Universeg: Universal medical image segmentation, 2023. 3
- [4] Cheng Chen, Juzheng Miao, Dufan Wu, Aoxiao Zhong, Zhiling Yan, Sekeun Kim, Jiang Hu, Zhengliang Liu, Lichao Sun, Xiang Li, Tianming Liu, Pheng-Ann Heng, and Quanzheng Li. Ma-sam: Modality-agnostic sam adaptation for 3d medical image segmentation. *Medical Image Analysis*, 98:103310, 2024. 3
- [5] Yiran Chen and et al. Mimo: A medical vision language model with visual referring multimodal input and pixel grounding multimodal output. *arXiv preprint arXiv:2408.07972*, 2024. 3
- [6] Zhe Chen and et al. Internvl: Scaling up vision foundation models and aligning for generic visual-linguistic tasks. In *CVPR*, pages 24185–24198. IEEE, 2024. 2, 4
- [7] Gabriel Comanici and et al. Gemini 2.5: Pushing the frontier with advanced reasoning, multimodality, long context, and next generation agentic capabilities. *arXiv preprint arXiv:2507.06261*, 2025. 2
- [8] Yuxin Du, Fan Bai, Tiejun Huang, and Bo Zhao. Segvol: Universal and interactive volumetric medical image segmentation. In *Advances in Neural Information Processing Systems 37 (NeurIPS 2024) — Main Conference Track*, 2024. 3, 8
- [9] Irem Ecenur Hamamci and et al. Developing generalist foundation models from a multimodal dataset for 3d computed tomography. *In Review*, 2024. 2, 3, 5, 7
- [10] Edward J. Hu, Yelong Shen, Phillip Wallis, Zeyuan Allen-Zhu, Yuanzhi Li, Shean Wang, Lu Wang, and Weizhu Chen. Lora: Low-rank adaptation of large language models, 2021. 4
- [11] Xinyu Huang and et al. Towards a multimodal large language model with pixel-level insight for biomedicine. *arXiv preprint arXiv:2408.02755*, 2024. 3
- [12] Alexander Kirillov, Eric Mintun, Nikhila Ravi, Hanzi Mao, Chloe Rolland, Laura Gustafson, Tete Xiao, Spencer Whitehead, Alexander C. Berg, Wan-Yen Lo, Piotr Dollár, and Ross Girshick. Segment anything, 2023. 3
- [13] Xuyang Lai and et al. Lisa: Reasoning segmentation via large language model. In *CVPR*, pages 9579–9589. IEEE, 2024. 2
- [14] Alon Lavie and Abhaya Agarwal. Meteor: an automatic metric for mt evaluation with high levels of correlation with human judgments. In *Proceedings of the Second Workshop on Statistical Machine Translation*, page 228–231, USA, 2007. Association for Computational Linguistics. 5
- [15] Changsun Lee, Sangjoon Park, Cheong-Il Shin, Woo Hee Choi, Hyun Jeong Park, Jeong Eun Lee, and Jong Chul Ye. Read like a radiologist: Efficient vision-language model for 3d medical imaging interpretation, 2024. 2, 3
- [16] Seowoo Lee, Jiwon Youn, Hyungjin Kim, Mansu Kim, and Soon Ho Yoon. Cxr-llava: a multimodal large language model for interpreting chest x-ray images, 2024. 5
- [17] Bo Li, Yuanhan Zhang, Dong Guo, Renrui Zhang, Feng Li, Hao Zhang, Kaichen Zhang, Peiyuan Zhang, Yanwei Li, Ziwei Liu, and Chunyuan Li. Llava-onevision: Easy visual task transfer, 2024. 2
- [18] Chunyuan Li, Cliff Wong, Sheng Zhang, Naoto Usuyama, Haotian Liu, Jianwei Yang, Tristan Naumann, Hoifung Poon, and Jianfeng Gao. Llava-med: Training a large language-and-vision assistant for biomedicine in one day. In *Proceedings of the 37th Conference on Neural Information Processing Systems (NeurIPS 2023) — Track on Datasets and Benchmarks*, 2023. 2, 5
- [19] Fuyu Li and et al. Llava-next-interleave: Tackling multi-image, video, and 3d in large multimodal models. *arXiv preprint arXiv:2409.17146*, 2024. 2
- [20] Junnan Li, Dongxu Li, Silvio Savarese, and Steven Hoi. Blip-2: Bootstrapping language-image pre-training with frozen image encoders and large language models. *arXiv preprint arXiv:2301.12597*, 2023. 2
- [21] Chin-Yew Lin. ROUGE: A package for automatic evaluation of summaries. In *Text Summarization Branches Out*, pages 74–81, Barcelona, Spain, 2004. Association for Computational Linguistics. 5
- [22] Jian Lin and et al. Vila: On pre-training for visual language models. *arXiv preprint arXiv:2306.00989*, 2023. 2
- [23] Tianwei Lin, Wenqiao Zhang, Sijing Li, Yuqian Yuan, Binhe Yu, Haoyuan Li, Wanggui He, Hao Jiang, Mengze Li, Xiaohui Song, Siliang Tang, Jun Xiao, Hui Lin, Yueling Zhuang, and Beng Chin Ooi. Healthgpt: A medical large vision-language model for unifying comprehension and generation via heterogeneous knowledge adaptation, 2025. 2

[24] Haotian Liu, Chunyuan Li, Qingyang Wu, and Yong Jae Lee. Visual instruction tuning. *arXiv preprint arXiv:2304.08485*, 2023. 2, 5

[25] Lingxiao Luo, Bingda Tang, Xuanzhong Chen, Rong Han, and Ting Chen. Vividmed: Vision language model with versatile visual grounding for medicine, 2025. 3

[26] Jun Ma, Yao Zhang, Song Gu, Cheng Zhu, Cheng Ge, Yichi Zhang, Xingle An, Congcong Wang, Qiyuan Wang, Xin Liu, Shucheng Cao, Qi Zhang, Shangqing Liu, Yunpeng Wang, Yuhui Li, Jian He, and Xiaoping Yang. Abdomenct-1k: Is abdominal organ segmentation a solved problem? *IEEE Transactions on Pattern Analysis and Machine Intelligence*, 44(10):6695–6714, 2022. 6

[27] Jun Ma, Yuting He, Feifei Li, Lin Han, Chenyu You, and Bo Wang. Segment anything in medical images. *Nature Communications*, 15(1), 2024. 3

[28] Jun Ma, Sumin Kim, Feifei Li, Mohammed Baharoon, Reza Asakereh, Hongwei Lyu, and Bo Wang. Segment anything in medical images and videos: Benchmark and deployment, 2024. 2, 3

[29] Michael Moor, Qian Huang, Shirley Wu, Michihiro Yasunaga, Yash Dalmia, Jure Leskovec, Cyril Zakka, Eduardo Pontes Reis, and Pranav Rajpurkar. Med-flamingo: a multimodal medical few-shot learner. In *Proceedings of the 3rd Machine Learning for Health Symposium*, pages 353–367. PMLR, 2023. 2

[30] Vishwesh Nath and et al. Vila-m3: Enhancing vision-language models with medical expert knowledge. *arXiv preprint arXiv:2405.19665*, 2024. 2, 3

[31] OpenAI and et al. Gpt-4o system card, 2024. 2

[32] Kishore Papineni, Salim Roukos, Todd Ward, and Wei-Jing Zhu. Bleu: a method for automatic evaluation of machine translation. In *Proceedings of the 40th Annual Meeting on Association for Computational Linguistics*, page 311–318, USA, 2002. Association for Computational Linguistics. 5

[33] Alec Radford, Jong Wook Kim, Chris Hallacy, Aditya Ramesh, Gabriel Goh, Sandhini Agarwal, Girish Sastry, Amanda Askell, Pamela Mishkin, Jack Clark, Gretchen Krueger, and Ilya Sutskever. Learning transferable visual models from natural language supervision, 2021. 3, 8

[34] Hanoona Rasheed and et al. Glamm: Pixel grounding large multimodal model. In *CVPR*, pages 13009–13018. IEEE, 2024. 2

[35] Nikhila Ravi, Valentin Gabeur, Yuan-Ting Hu, Ronghang Hu, Chaitanya Ryali, Tengyu Ma, Haitham Khedr, Roman Rädle, Chloe Rolland, Laura Gustafson, Eric Mintun, Junting Pan, Kalyan Vasudev Alwala, Nicolas Carion, Chao-Yuan Wu, Ross Girshick, Piotr Dollár, and Christoph Feichtenhofer. Sam 2: Segment anything in images and videos, 2024. 3

[36] Blaine Rister, Darvin Yi, Kaushik Shivakumar, Tomomi Nobashi, and Daniel L. Rubin. Ct-org, a new dataset for multiple organ segmentation in computed tomography. *Scientific Data*, 7(1):381, 2020. 6

[37] Tal Shaharabany, Aviad Dahan, Raja Giryes, and Lior Wolf. Autosam: Adapting sam to medical images by overloading the prompt encoder, 2023. 3

[38] Yiming Shi, Xun Zhu, Kaiwen Wang, Ying Hu, Chenyi Guo, Miao Li, and Ji Wu. Med-2e3: A 2d-enhanced 3d medical multimodal large language model, 2025. 2, 3

[39] Ilya Tolstikhin, Neil Houlsby, Alexander Kolesnikov, Lucas Beyer, Xiaohua Zhai, Thomas Unterthiner, Jessica Yung, Andreas Steiner, Daniel Keysers, Jakob Uszkoreit, Mario Lucic, and Alexey Dosovitskiy. Mlp-mixer: An all-mlp architecture for vision, 2021. 4

[40] Shengbang Tong, Ellis Brown, Penghao Wu, Sanghyun Woo, Manoj Middepogu, Sai Charitha Akula, Jihan Yang, Shusheng Yang, Adithya Iyer, Xichen Pan, Austin Wang, Rob Fergus, Yann LeCun, and Saining Xie. Cambrian-1: A fully open, vision-centric exploration of multimodal llms. In *Advances in Neural Information Processing Systems 37 (NeurIPS 2024) — Main Conference Track*, 2024. 5

[41] Ramakrishna Vedantam, C. Lawrence Zitnick, and Devi Parikh. Cider: Consensus-based image description evaluation. In *Proceedings of the IEEE Conference on Computer Vision and Pattern Recognition (CVPR)*, pages 4566–4575, 2015. 5

[42] Jakob Wasserthal, Hanns-Christian Breit, Manfred T. Meyer, Maurice Pradella, Daniel Hinck, Alexander W. Sauter, Tobias Heye, Daniel T. Boll, Joshy Cyriac, Shan Yang, Michael Bach, and Martin Segeroth. Totalsegmentator: Robust segmentation of 104 anatomic structures in ct images. *Radiology: Artificial Intelligence*, 5(5):e230024, 2023. 6

[43] Chaoyi Wu, Xiaoman Zhang, Ya Zhang, Hui Hui, Yanfeng Wang, Weidi Xie, et al. Towards generalist foundation model for radiology by leveraging web-scale 2d&3d medical data. *Nature Communications*, 16(1):7866, 2025. 2

[44] Junde Wu, Wei Ji, Yuanpei Liu, Huazhu Fu, Min Xu, Yanwu Xu, and Yueming Jin. Medical sam adapter: Adapting segment anything model for medical image segmentation, 2023. 3

[45] Yunfei Xie, Ce Zhou, Lang Gao, Juncheng Wu, Xianhang Li, Hong-Yu Zhou, Sheng Liu, Lei Xing, James Zou, Cihang Xie, and Yuyin Zhou. Medtrinity-25m: A large-scale multimodal dataset with multigranular annotations for medicine, 2025. 2

[46] Yang Xin, Gorkem Can Ates, Kun Gong, and Weitian Shao. Med3dvlm: An efficient vision-language model for 3d medical image analysis. *arXiv preprint arXiv:2503.20047*, 2025. 2, 3

[47] Chenyang Yan and et al. Visa: Reasoning video object segmentation via large language models. In *ECCV*, pages 98–115. Springer Nature Switzerland, 2025. 2

[48] An Yang, Anfeng Li, Baosong Yang, Beichen Zhang, Binyuan Hui, Bo Zheng, Bowen Yu, Chang Gao, Chengen Huang, Chenxu Lv, Chujie Zheng, Dayiheng Liu, Fan Zhou, Fei Huang, Feng Hu, Hao Ge, Haoran Wei, Huan Lin, Jialong Tang, Jian Yang, Jianhong Tu, Jianwei Zhang, Jianxin Yang, Jiaxi Yang, Jing Zhou, Jingren Zhou, Junyang Lin, Kai Dang, Keqin Bao, Kexin Yang, Le Yu, Lianghao Deng, Mei Li, Mingfeng Xue, Mingze Li, Pei Zhang, Peng Wang, Qin Zhu, Rui Men, Ruize Gao, Shixuan Liu, Shuang Luo, Tianhao Li, Tianyi Tang, Wenbiao Yin, Xingzhang Ren, Xinyu Wang, Xinyu Zhang, Xuancheng Ren, Yang Fan, Yang Su,

Yichang Zhang, Yinger Zhang, Yu Wan, Yuqiong Liu, Zekun Wang, Zeyu Cui, Zhenru Zhang, Zhipeng Zhou, and Zihan Qiu. Qwen3 technical report, 2025. [2](#)

[49] Yunhan Yang, Xiaoyang Wu, Tong He, Hengshuang Zhao, and Xihui Liu. Sam3d: Segment anything in 3d scenes, 2023. [3](#)

[50] Haotian You and et al. Ferret: Refer and ground anything anywhere at any granularity. *arXiv preprint arXiv:2312.06647*, 2023. [2](#)

[51] Haolin Yuan and et al. Sa2va: Marrying sam2 with llava for dense grounded understanding of images and videos. *arXiv preprint arXiv:2501.04001*, 2025. [2](#), [5](#)

[52] Hongbo Zhang, Junying Chen, Feng Jiang, Fei Yu, Zhi-hong Chen, Jianquan Li, Guiming Chen, Xiangbo Wu, Zhiyi Zhang, Qingying Xiao, Xiang Wan, Benyou Wang, and Haizhou Li. Huatuogpt, towards taming language model to be a doctor, 2023. [2](#)

[53] Haotian Zhang, Haoxuan You, Philipp Dufter, Bowen Zhang, Chen Chen, Hong-You Chen, Tsu-Jui Fu, William Yang Wang, Shih-Fu Chang, Zhe Gan, and Yinfei Yang. Ferret-v2: An improved baseline for referring and grounding with large language models, 2024. [2](#)

[54] Tianyi Zhang, Varsha Kishore, Felix Wu, Kilian Q. Weinberger, and Yoav Artzi. Bertscore: Evaluating text generation with bert, 2020. [5](#)

[55] Theodore Zhao, Yu Gu, Jianwei Yang, Naoto Usuyama, Ho Hin Lee, Sid Kiblawi, Tristan Naumann, Jianfeng Gao, Angela Crabtree, Jacob Abel, Christine Moung-Wen, Brian Piening, Carlo Bifulco, Mu Wei, Hoifung Poon, and Sheng Wang. A foundation model for joint segmentation, detection and recognition of biomedical objects across nine modalities. *Nature Methods*, 22(1):166–176, 2025. [2](#), [3](#)

MedVL-SAM2: A unified 3D medical vision–language model for multimodal reasoning and prompt-driven segmentation

Supplementary Material

Table 8. Module parameters and model size

Module	Parameters	Size
Vision Encoder	198.05M	377.76 MB
Projection Layer	7.09M	13.52 MB
LLM Backbone	3.39B	6.33 GB
Segmentation Module	224.43M	428.07 MB
Total	3.82B	7.15 GB

8. Training Details

Detailed module parameters of the proposed method are presented in Table 8. 8 NVIDIA B200 GPUs were used for training and 1 B200 GPU was used for evaluation. For training Stages 1 and 2, where the trainable parameters did not include SAM2 modules, the batch size was set to 16 per GPU (effective batch size 128). Training Stage 1 for vision-language alignment required approximately 6 hours over 3 epochs, while training Stage 2, which strengthened language reasoning, required approximately 18 hours over 5 epochs. For training Stage 3 involving joint-training, the batch size was set to 1 per GPU with 8-step gradient accumulation (effective batch size 8). The entire joint-training process required approximately 110 hours over 10 epochs.

Loss function hyperparameters for Stage 3 were set as follows: $\lambda_{text} = 0.5$, $\lambda_{mask} = 2.0$, and $\lambda_{Dice} = 1.0$. These values were determined through validation set tuning.

9. Prompt Templates for Different Tasks

We utilize task-specific prompts and templates to guide the LLM across different tasks, including report generation, semantic segmentation, and referring segmentation. Figure 5 shows prompts for report generation, while Figures 6, 7, and 8 present instruction templates for segmentation tasks.

10. Qualitative Results: Report Generation

Examples of report generation are presented in Figure 9. Different aspects of the generated reports are color-coded for clarity: clinical findings in orange, COVID-19 related findings in blue, normal/healthy findings in green, and diagnostic conclusions in red.

11. Qualitative Results: Segmentation Tasks

Examples of segmentation tasks on the ACT-1K dataset are presented in Figure 10. We observe that, for relatively sim-

Report Generation:
<ul style="list-style-type: none">• "Can you generate the report for the following chest CT image?",• "Please provide the radiology report for the chest CT image mentioned.",• "I need the radiology report for the given chest CT image.",• "Could you create a report for this chest CT scan?",• "Would you mind generating the radiology report for the specified chest CT image?",• "Please generate the report for the chest CT image provided.",• "Can you produce the radiology report for the attached chest CT image?",• "I need a detailed report for the given chest CT image.",• "Could you write the radiology report for this chest CT scan?",• "Please give the radiology report for the specified chest CT image.",• "Generate radiology report for the CT.",• "Produce the report for this CT image.",• "Write a radiology report for the following CT scan.",• "Create a report for this chest CT.",• "Provide the radiology report for this CT image.",• "Can you generate the report for the following chest CT volume?",• "Please provide the radiology report for the chest CT volume mentioned.",• "I need the radiology report for the given chest CT volume.",• "Could you create a report for this chest CT volume?",• "Would you mind generating the radiology report for the specified chest CT volume?",• "Please generate the report for the chest CT volume provided.",• "Can you produce the radiology report for the attached chest CT volume?",• "I need a detailed report for the given chest CT volume.",• "Could you write the radiology report for this chest CT volume?",• "Please give the radiology report for the specified chest CT volume.",• "Generate radiology report for the CT volume.",• "Produce the report for this CT volume.",• "Write a radiology report for the following CT volume.",• "Create a report for this chest CT volume.",• "Provide the radiology report for this CT volume.",• "Can you generate the report for the following chest CT scan?",• "Please provide the radiology report for the chest CT scan mentioned.",• "I need the radiology report for the given chest CT scan.",• "Could you create a report for this chest CT scan?",• "Would you mind generating the radiology report for the specified chest CT scan?",• "Please generate the report for the chest CT scan provided.",• "Can you produce the radiology report for the attached chest CT scan?",• "I need a detailed report for the given chest CT scan.",• "Could you write the radiology report for this chest CT scan?",• "Please give the radiology report for the specified chest CT scan.",• "Generate radiology report for the CT scan.",• "Produce the report for this CT scan.",• "Write a radiology report for the following CT scan.",• "Provide the radiology report for this CT scan."

Figure 5. Prompt templates used for report generation tasks.

ple cases involving large organs such as the liver and spleen, bounding box prompts provide minimal performance improvement since the results from referring and semantic segmentation are already sufficient. However, for challenging cases involving smaller or more complex structures such as the kidneys and pancreas, bounding box prompts provide additional spatial cues that significantly improve segmentation accuracy.

Semantic Segmentation:

Questions:

- "Can you segment the {class_name} in this image?",
- "Please segment {class_name} in this image.",
- "What is {class_name} in this image? Please respond with segmentation mask.",
- "What is {class_name} in this image? Please output segmentation mask.",
- "Can you segment the {class_name} in this image?",
- "Please segment {class_name} in this image",
- "What is {class_name} in this image? Please respond with segmentation mask",
- "What is {class_name} in this image? Please output segmentation mask",
- "Could you provide a segmentation mask for the {class_name} in this image?",
- "Please identify and segment the {class_name} in this image.",
- "Where is the {class_name} in this picture? Please respond with a segmentation mask.",
- "Can you highlight the {class_name} in this image with a segmentation mask?",
- "Could you provide a segmentation mask for the {class_name} in this image?",
- "Please identify and segment the {class_name} in this image",
- "Where is the {class_name} in this picture? Please respond with a segmentation mask",
- "Can you highlight the {class_name} in this image with a segmentation mask"

Answers:

- "It is [SEG].",
- "Sure, [SEG].",
- "Sure, it is [SEG].",
- "Sure, the segmentation result is [SEG].",
- "[SEG]."

Figure 6. Prompt templates used for semantic segmentation tasks.

Semantic Segmentation:

Questions:

- "{} Please answer and segment.",
- "{} Please output segmentation mask and answer.",
- "{} Please answer and segment based on the above description.",
- "{} Please answer and segment based on the above definition.",
- "{} Can you answer and segment it based on the above description or definition.",
- "{} Please output segmentation mask and answer based on the above description or definition.",
- "{} Please segment accordingly.",
- "{} Please provide segmentation and answer according to it.",
- "{} Now, segment it and provide your answer.",
- "{} Please segment and provide your response.",
- "{} Can you segment it accordingly?",
- "Description: {} Please answer and segment based on the above description.",
- "Definition: {} Please answer and segment based on the above definition.",
- "Description: {} Can you answer and segment it based on the above description or definition.",
- "Definition: {} Please output segmentation mask and answer based on the above description or definition.",
- "Provided description: {} Please segment accordingly.",
- "Given definition: {} Please provide segmentation and answer according to it.",
- "The description provided is: {} Now, segment it and provide your answer.",
- "Based on the provided definition: {} Please segment and provide your response.",
- "Describing the object as: {} Can you segment it accordingly?",
- "Defining it as: {} Now, segment and provide your answer.",

Answers:

- "The target is {} and the segmentation mask is [SEG].",
- "The category is {} and the mask is [SEG].",
- "It is {}, [SEG].",
- "{} [SEG]",
- "Identified as {}, here is the segmentation: [SEG].",
- "Categorized as {}, the segmentation is: [SEG].",
- "The class is {}, and the corresponding segmentation is: [SEG].",
- "Regarding the classification, it is {}, and the segmentation is: [SEG].",
- "Classified as {}, here's the segmentation: [SEG].",
- "The label assigned is {}, and the associated segmentation is: [SEG].",
- "Category: {}, segmentation: [SEG].",
- "It's classified as {}, with the segmentation: [SEG]."

Figure 7. Prompt templates used for referring segmentation tasks.

Term Dictionary:

Kidneys:

- "Primary organ responsible for detoxifying the blood by removing harmful substances.",
- "Produces bile, a fluid that aids in the digestion and absorption of fats.",
- "Stores and regulates glycogen, a crucial energy reserve for the body.",
- "Synthesizes proteins necessary for blood clotting and immune system function.",
- "Plays a central role in metabolism, including the breakdown of carbohydrates and fats.",
- "Large organ in the upper right abdomen with various metabolic functions.",
- "Produces bile for digestion, detoxifies blood, and stores glycogen.",
- "Essential for metabolic processes and nutrient storage.",
- "Regenerates and repairs damaged tissue.",
- "Common site for conditions such as hepatitis and cirrhosis."

Liver:

- "Primary organ responsible for detoxifying the blood by removing harmful substances.",
- "Produces bile, a fluid that aids in the digestion and absorption of fats.",
- "Stores and regulates glycogen, a crucial energy reserve for the body.",
- "Synthesizes proteins necessary for blood clotting and immune system function.",
- "Plays a central role in metabolism, including the breakdown of carbohydrates and fats.",
- "Large organ in the upper right abdomen with various metabolic functions.",
- "Produces bile for digestion, detoxifies blood, and stores glycogen.",
- "Essential for metabolic processes and nutrient storage.",
- "Regenerates and repairs damaged tissue.",
- "Common site for conditions such as hepatitis and cirrhosis.",
- "Large organ located in the upper right abdomen with various metabolic functions.",

Brain:

- "Central organ of the nervous system responsible for cognition and control of bodily functions.",
- "Complex organ housed within the skull responsible for processing sensory information and controlling body functions.",
- "Command center of the nervous system responsible for processing information and coordinating bodily activities.",
- "Highly organized mass of nerve tissue enclosed within the skull responsible for cognitive functions and regulating body processes.",

Lungs:

- "Organs responsible for respiration.",
- "Respiratory organs facilitating gas exchange.",
- "Pair of organs involved in breathing.",
- "Primary respiratory structures in the body.",
- "Organs essential for oxygen exchange.",
- "Respiratory structures enabling air intake and release.",
- "Pair of vital organs for oxygenation.",
- "Main organs for inhaling and exhaling air.",

Spleen:

- "Organ located in the upper left abdomen, part of the lymphatic system.",
- "Filters blood, removing damaged blood cells and pathogens.",
- "Stores platelets and white blood cells.",
- "Involved in immune response and blood filtration.",
- "Can be affected by conditions like splenomegaly or ruptured spleen.",
- "Organ located in the upper left abdomen, part of the lymphatic system.",
- "Filters blood, removing damaged blood cells and pathogens.",
- "Organ located in the upper left abdomen, part of the lymphatic system.",
- "Organ in the lymphatic system located in the upper left abdomen.",

Figure 8. Anatomical descriptions used as free-form text prompts for referring segmentation tasks. These descriptions replace the {} placeholder in the templates shown in Figure 7.

Report Generation	
	<p><Ground Truth>: Findings: Trachea and both main bronchi are open. No occlusive pathology was detected in the trachea and both main bronchi. Central and peripheral consolidations and ground glass areas are observed in the middle lobe and lower lobe of the right lung. There are also small areas of ground glass and nodular-shaped consolidations in the left lung. The described findings were evaluated in favor of viral pneumonia. Findings described especially in the right lung are frequently encountered findings in Covid-19 pneumonia. No mass was detected in both lungs. Mediastinal structures cannot be evaluated optimally because contrast material is not given. As far as can be observed: Heart contour and size are normal. No pleural or pericardial effusion was detected. The widths of the mediastinal main vascular structures are normal. No enlarged lymph nodes in pathological size and appearance were detected in the mediastinum and hilar regions. No pathological wall thickness increase was observed in the esophagus within the sections. No upper abdominal free fluid-collection was detected in the sections. No pathologically enlarged lymph nodes were observed. In the upper abdominal organs within the sections, there is no mass with distinguishable borders as far as it can be observed within the borders of non-enhanced CT. Thoracic vertebral corpus heights, alignments and densities are normal. Intervertebral disc distances are preserved. The neural foramina are open. No lytic-destructive lesions were detected in the bone structures within the sections. Impression: Findings evaluated in favor of viral pneumonia in both lungs</p>
	<p><Our model>: Findings: Trachea and main bronchi are open. No pathological lymph node was detected in the mediastinum. The heart and mediastinal vascular structures have a natural appearance. Esophagus is within normal limits. Pleural effusion-thickening was not detected in both hemithorax. In the evaluation of both lung parenchyma: Patchy, peripheral-subpleural, ground glass density, crazy paving appearances and consolidations were observed in both lungs. Viral pneumonia? There are cylindrical bronchiectasis and vascular enlargement in the affected areas. CT involvement score was evaluated as mild. In the sections passing through the upper part of the abdomen, the bilateral adrenal glands appear natural. No significant pathology was detected in the abdominal sections. No obvious pathology was detected in bone structures. Impression: Viral pneumonia? Outlooks include classic or probable findings for COVID. Note: Other infectious agents such as influenza, parainfluenza, mycoplasma, other organized pneumonias such as drug toxicity, connective tissue diseases should be considered in the differential diagnosis as they may cause similar appearances.</p>
	<p><CT-CHAT>: Findings: Trachea and main bronchi are open. No pathological lymph node was detected in the mediastinum. The heart and mediastinal vascular structures have a natural appearance. Esophagus is within normal limits. Pleural effusion-thickening was not detected in both hemithorax. In the evaluation of both lung parenchyma: No suspicious nodule, mass or infiltration was detected in both lungs. In the sections passing through the upper part of the abdomen, the bilateral adrenal glands appear natural. No significant pathology was detected in the abdominal sections. No obvious pathology was detected in bone structures. Impression: No signs of infection were detected in the lungs. However, it should be known that CT may be false negative in the first few days. Clinical and laboratory evaluation will be appropriate.</p>

Figure 9. Qualitative comparison of the proposed method with CT-Chat on the report generation task. Coronal, axial, and sagittal views of the corresponding CT scans are shown. Different aspects of the reports are color-coded for improved readability.

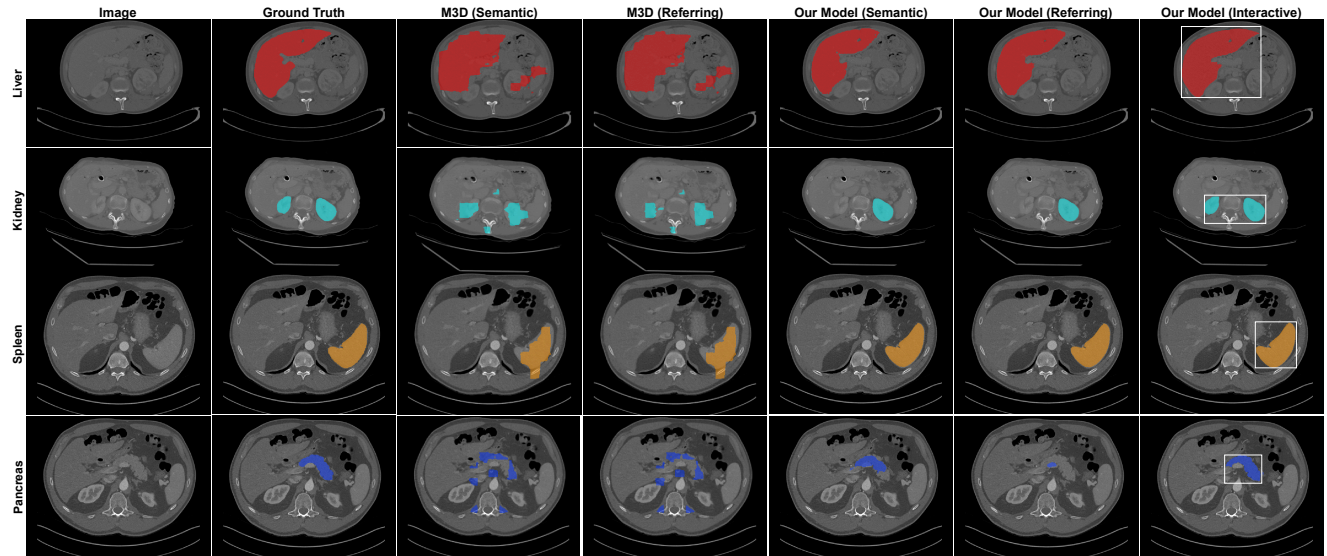


Figure 10. Qualitative comparison of the proposed method with M3D on referring and semantic segmentation. Interactive segmentation results using bounding-box prompts are also included for comparison (ACT-1K dataset). The liver is shown in red, the kidney in cyan, the spleen in orange, and the pancreas in blue.